Myoglobin-CO Conformational Substate Dynamics: 2D Vibrational Echoes and MD Simulations

Kusai A. Merchant,* David E. Thompson,* Qing-Hua Xu,* Ryan B. Williams,[†] Roger F. Loring,[†] and Michael D. Fayer*

*Department of Chemistry, Stanford University, Stanford, California 94305 and [†]Department of Chemistry and Chemical Biology, Baker Laboratory Cornell University, Ithaca, New York 14853 USA

ABSTRACT   Two-dimensional (2D) infrared vibrational echoes were performed on horse heart carbonmonoxymyoglobin (MbCO) in water over a range of temperatures. The A_1 and A_3 conformational substates of MbCO are found to have different dephasing rates with different temperature dependences. A frequency–frequency correlation function derived from molecular dynamics simulations on MbCO at 298 K is used to calculate the vibrational echo decay. The calculated decay shows substantial agreement with the experimentally measured decays. The 2D vibrational echo probes protein dynamics and provides an observable that can be used to test structural assignments for the MbCO conformational substates.

INTRODUCTION

Protein dynamics have been the focus of both intense theoretical and experimental study for over 25 years. In particular, a tremendous amount of work has focused on myoglobin (Mb), a small globular protein involved in the storage of oxygen. Over 50 years ago, sperm whale myoglobin was the first protein to be characterized structurally with x-ray crystallography (Kendrew, 1948), and continued refinements of protein structures from x-ray (Kuriyan et al., 1986; Vojtechovsky et al., 1999) and neutron scattering (Cheng and Schoenborn, 1991) have yielded structures with atomic resolution. From a functional standpoint, the reversible binding of small molecule ligands, such as O_2, CO, and NO, represents one of the simplest chemical actions of a protein. Because of its relatively small size, structural calculations and molecular dynamics simulations on myoglobin are tractable with modern computers and algorithms (Elber and Karplus, 1987; Meller and Elber, 1998; Sagnella et al., 1999; Rovira et al., 2001; Williams et al., 2001). These factors make myoglobin an ideal system to test ideas about protein dynamics, structure, and function.

Most biological processes occur on the ground state of the electronic potential energy surface. This fact makes the study of the vibrational dynamics of proteins particularly relevant because vibrational dynamics reflect thermal motions of the mechanical degrees of freedom. The spin echo of nuclear magnetic resonance (NMR) (Hahn, 1950) has long been recognized as a powerful technique for providing structural and dynamical information on molecules. By providing structural maps of proteins in solution, multidimensional NMR techniques, (Bodenhausen et al., 1978;

Schmidt-Rohr and Spiess, 1994), which are multiple pulse extensions of the spin echo, have provided insight into the relatively slow global motions and structure of proteins (Lukin et al., 2000). However, under most circumstances, the inherent time resolution of NMR techniques is limited to the microsecond regime. These time scales are important in understanding the collective motions of large parts of proteins, but can provide little information about structural motions that occur on faster time scales. Because collective motions on long time scales arise from the fast, relatively local motions on short time scales, it is desirable to measure and understand these fast motions.

The vibrational echo (Zimdars et al., 1993; Hamm et al., 1998) is the infrared (IR) analog of the spin echo in NMR (Hahn, 1950) and the photon echo (Abella et al., 1966) in electronic excited state spectroscopy. The two-pulse vibrational echo is a time-domain technique used to measure the dynamics associated with the interaction between a particular vibrational mode and its surrounding environment. Linear IR spectroscopy measures a line shape with contributions from the vibrational lifetime, and from pure dephasing dynamics with a wide range of associated time scales. Like the NMR spin echo, the vibrational echo provides dynamical information by eliminating inhomogeneous broadening caused by slow processes. The lifetime contribution to the spectroscopic line can also be separated from the dynamical line shape by measuring the vibrational lifetime with time dependent IR pump-probe spectroscopy, and then subtracting the vibrational lifetime contribution from the echo decay. This allows one to study the pure dephasing processes, which give direct information about the nature of the interaction of an oscillator with its environment. Vibrational echo techniques have recently been extended to multiple dimensions, which can provide structural and dynamical information for complex molecules (Golonzka et al., 2001; Thompson et al., 2001; Zanni et al., 2001). However, unlike NMR, the vibrational echo has an inherent time resolution on the order of tens of femtoseconds, making

it an ideal tool to probe the fast mechanical motions in molecules.

SPECTROSCOPY OF MYOGLOBIN-CO

The IR absorption spectrum of the CO stretch of horse heart carbonmonoxymyoglobin (MbCO) shows that MbCO exists in at least three spectroscopically distinct conformational substates: the A_0 state centered at $\sim$1965 cm^{-1}, the A_1 state at $\sim$1944 cm^{-1}, and the A_3 state at $\sim$1935 cm^{-1} (the initial proposal for the existence of an A_2 state has fallen out of fashion) (Caughey et al., 1981; Shimada and Caughey, 1982; Hong et al., 1990; Johnson et al., 1996; Müller et al., 1999). These substates are thought to correspond to different interconverting structures of the protein, possibly with different biological functionality. For example, the protein structural conformations corresponding to the A_0 and A_1 substates may play a role in controlling the rate of oxygen uptake in muscle tissue (Miller et al., 1996). The interconversion times between the A_1 and A_3 substates are $\sim$1 ns, whereas the interconversion time between the A_0 and $A_1 \leftrightarrow A_3$ substates is $\sim$1 μs (Johnson et al., 1996). These interconversion rates are too fast to be resolved using NMR (Caughey et al., 1981) but are essentially static on the vibrational echo timescale. Various hypotheses for the structural identities of these substates have recently been reviewed (Rovira et al., 2001).

Recently, one dimensional (1D) vibrational echo experiments on the CO stretch of MbCO and several mutants with substitutions near the active site were performed over a wide range of temperatures and viscosities in a variety of solvents (Rector et al., 1997b, 1998, 1999, 2001). The CO stretch in MbCO is an ideal spectroscopic probe in the IR. In contrast to the amide I band, where it is not possible to assign a particular transition frequency to a particular residue, the CO stretch is spectroscopically isolated and spatially localized. However, despite its spatial localization, the CO stretch is quite sensitive to global motions of the protein. The temperature-dependent (Rector et al., 1999) and viscosity-dependent (Rector et al., 2001) experiments show the vibrational dephasing rate of the CO stretch to be highly sensitive to both temperature and solvent viscosity, and that increases in temperature and decreases in viscosity both lead to an increased dephasing rate. The mutant studies indicate that the CO vibrational dephasing rate is sensitive to electric field fluctuations produced by global protein motions, and not necessarily to through-bond interactions between the CO and protein (Rector et al., 1997b, 1998). Increasing the temperature produces larger amplitude thermal motions of the protein and a decrease in the solvent viscosity. Decreasing the viscosity reduces topological constraints on protein surface motions, making the protein backbone become less rigid. Both processes increase the amplitude and decrease the time scale of protein dynamics, leading to a more rapid decay of the vibrational echo signal.

The temperature-dependent and viscosity-dependent vibrational echo experiments on MbCO demonstrate the capacity of CO to be used as a spectroscopic reporter of global protein dynamics.

These 1D vibrational echo experiments on MbCO (Rector et al., 1997b, 1998, 1999, 2001) were performed using laser pulses with a duration of $\sim$1 ps and bandwidth of $\sim$15 cm^{-1} tuned to the A_1 substate. At biologically relevant temperatures, the 1D vibrational echo decay shapes were strongly influenced by the pulse duration and contained substantial contributions from the A_3 substate. In the present work, two-dimensional (2D) spectrally resolved vibrational echo spectroscopy is used for the first time to study separately the A_1 and A_3 substates of horse heart MbCO over a range of temperatures with high time and frequency resolution. The A_3 substate vibrational echo decay is more rapid than the A_1 substate decay and shows a weak temperature dependence. The A_1 vibrational echo decay shows a more pronounced dependence on temperature. Both decay curves are nonexponential.

The dynamical times scales relevant to vibrational echoes in MbCO are readily accessed in a molecular dynamics simulation (Elber and Karplus, 1987; Meller and Elber, 1998; Schulze and Evanseck, 1999; Rovira et al., 2001). Algorithms for the calculation of the vibrational echo observable from classical mechanical simulation data have recently been investigated (Williams and Loring, 2000a,b; Akiyama and Loring, 2002). Within the fluctuating frequency approximation (Williams and Loring, 2000b; Akiyama and Loring, 2002), the echo signal may be related to the time-dependent vibrational frequency fluctuation of CO. With the further assumption of a solvent obeying Gaussian statistics, the echo observable can be calculated from the autocorrelation function of this frequency fluctuation. Loring and coworkers have calculated and analyzed the frequency–frequency correlation function (FFCF) for sperm whale MbCO in water at room temperature (Williams et al., 2001). In the present work, we use this simulated FFCF to calculate the vibrational echo observable. We show that the results are in substantial agreement with laboratory data, despite the absence of any adjustable parameters in the comparison. It is far from clear that conventional force fields used in molecular dynamics simulations of biomolecules can reproduce the amplitudes and time scales of the structural fluctuations measured in the echo experiment. The combination of molecular dynamics simulations and ultrafast IR vibrational dynamics studies represents a powerful new approach to understanding and testing detailed models of protein motion and structure.

EXPERIMENTAL PROCEDURES

The ultrafast IR vibrational echo is a nonlinear optical time-domain technique used to study vibrational dynamics by measuring the dephasing rate of an oscillator (Rector and

Fayer, 1998). In these experiments, a short pulse of IR laser light tuned to the transition frequency (~5 μm) with wave vector $\vec{k}_1$ is passed through the sample, creating a macroscopic polarization that undergoes a free induction decay. After a time τ, a second laser pulse with wave vector $\vec{k}_2$ is passed through the sample, which initiates a rephasing process in the oscillators, leading to another macroscopic polarization maximum in the sample at time ~2τ. This macroscopic polarization radiates in the $2\vec{k}_2 - \vec{k}_1$ phase-matched direction, and generates the vibrational echo signal. As τ, the delay between the pulses, is increased, generally the intensity of the vibrational echo signal decreases, although the overall decay can have oscillations. The decay of the vibrational echo signal as a function of τ is related to the Fourier transform of the dynamical spectroscopic line (Berg et al., 2000).

The experimental apparatus has been described in detail elsewhere (Thompson et al., 2001). Briefly, tunable mid-IR pulses with a center frequency of ~1940 cm^{-1} were generated by an optical parametric amplifier pumped with a regeneratively amplified Ti:Sapphire laser. The bandwidths and pulse durations used in these experiments were 100 cm^{-1} and 150 fs (2D data at 298 K) or 130 cm^{-1} and 110 fs (1D data at all temperatures and 2D data at 279 K and 320 K), respectively. A 15%/85% ZnSe beam splitter was used to create a weak beam ($\vec{k}_1$) and strong beam ($\vec{k}_2$). In a two-pulse vibrational echo experiment, the signal intensity is linear in the intensity of the first pulse and quadratic in the intensity of the second pulse. Therefore, it is advantageous to have the second pulse more intense than the first pulse. Furthermore, to perform a pump-probe measurement of the vibrational lifetime, the probe pulse should be weak compared to the pump pulse. The 15%/85% ZnSe beam splitter makes it possible to do both experiments without changing optics. The timing between the two beams was controlled by passing the weak beam down a computer-controlled delay line. The beams were crossed and focused at the sample with a 6-in off-axis parabolic reflector. The vibrational echo pulse, generated in the $2\vec{k}_2 - \vec{k}_1$ phase-matched direction, was detected with a liquid nitrogen-cooled HgCdTe detector (1D vibrational echo) or dispersed in a monochromator and then detected (2D vibrational echo). The 2D spectrum is generated by stepping the monochromator and scanning the delay between the pulses and recording the vibrational echo decay at each frequency. The resolution of the monochromator was 1.25 cm^{-1} for the 298 K data and 3 cm^{-1} for the 279 and 320 K data. The parent pulse energy was ~3 μJ/pulse, and the spot size at the sample was ~150 μm. A power-dependence study was performed, and the data showed no power-dependent effects.

Horse heart myoglobin (Sigma Corp., St. Louis, MO) was dissolved in pH 7, 0.1 M phosphate buffer, centrifuged to remove large particulates, and then purged with nitrogen to remove dissolved oxygen. The myoglobin solution was reduced with excess dithionite solution and stirred under a
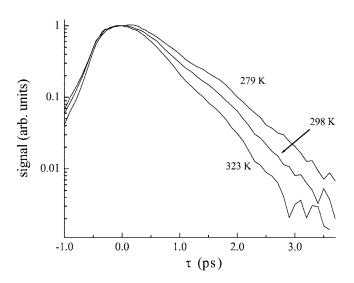

FIGURE 1 One-dimensional temperature-dependent vibrational echo decays. The 1D vibrational echo decay rates at 279, 298, and 323 K show a clear increase as the temperature is raised. The decays appear exponential, that is, they are linear on the semi-log plot. The oscillations in the data are real, see text.

CO atmosphere for an hour before being filtered with a 0.45-μm acetate filter and placed in a custom gas-tight 50-μm copper sample cell with CaF$_2$ windows. The sample temperature was controlled with a continuous-flow cryostat and monitored with a silicon diode temperature sensor bonded to one of the CaF$_2$ windows.

RESULTS

One dimensional MbCO vibrational echo decays were measured at 279, 298, and 323 K. The three vibrational echo decays are shown in Fig. 1. The data show an increase in the vibrational echo decay rate as the temperature is increased. The vibrational echoes appear exponential over three decades of signal decay. (There are deviations from a straight line in the data that are real oscillations caused by accidental degeneracy beats that occur at the frequency of the vibrational anharmonicity, that is, the difference in the frequency of the 0–1 and 1–2 vibrational transitions (Merchant et al., 2001, 2002). In general, the vibrational echo decay rate has contributions from two types of dephasing processes. The first of these is vibrational relaxation (population decay), and the second is pure dephasing (Tokmakoff and Fayer, 1995). Pure dephasing processes are adiabatic fluctuations in the transition frequency of an oscillator that are the result of interactions between the oscillator and its environment. MbCO vibrational lifetime measurements in this and previous work (Rector and Fayer 1999) demonstrate that the dominant contribution to the overall dephasing rate at the experimental temperatures is pure dephasing. An exponential decay of the vibrational echo signal often implies that the oscillator has an extremely rapidly decaying FFCF

(Kubo 1961). In this case, the dynamics of the oscillator are typically discussed within the context of motional narrowing. The dynamical spectroscopic line shape is Lorentzian, and the width of the line is equal to $1/(\pi \times$ dephasing rate). These simple relations between the echo observable and the dynamics of the system were first explained by Kubo (1961) in the context of NMR.

Because the bandwidth of the laser pulses used in the 1D experiments presented here is ~ 100 cm^{-1}, the 1D decays have contributions from all three A substates. In addition, the laser bandwidth exceeds the CO stretch anharmonicity of 25 cm^{-1}, resulting in signal contributions from 1–2 vibrational transitions (see Appendix A). The 1D vibrational echo decays shown in Fig. 1 have, in principle, six contributions, that is, contributions from the 0–1 transitions of the A_0, A_1, and A_3 substates, and contributions from the 1–2 transitions of each of these substates. It is possible that each of these six transitions will give rise to a distinct decay. The signal is observed at the intensity level, which is the absolute squared of the polarization level signal. When the signal is observed, it not only is composed of six decays, it also has cross terms between the various decays. Thus, the seemingly simple 1D decay is a superposition of many decays.

Two-dimensional vibrational echo spectroscopy makes it possible to resolve these various contributions into their individual components and measure each one separately. In the 2D experiment, the vibrational echo signal is spectrally resolved. The 2D signal is a function of both the delay between the pulses and the detection frequency. The background-subtracted linear absorption spectrum for horse heart MbCO is shown in Fig. 2 a. Figure 2 b shows the results of fitting the absorption spectrum to 3 bands, A_0, A_1, and A_3 (*solid lines*). The fit was performed using three Voigt line shapes and the approximate known center frequencies of the three bands (Caughey et al., 1981; Shimada and Caughey, 1982; Hong et al., 1990; Johnson et al., 1996). The A_0 band was fit to a Gaussian line shape (the Lorentzian component of the Voigt line shape was zero). The A_1 and A_3 line shape have significant Lorentzian components. As discussed below, the A_1 and A_3 vibrational echo decays are not exponential, and, therefore, the dynamical line shape is not strictly Lorentzian. Thus, in this situation, the Lorentzian and Gaussian linewidths obtained from the fits of the A_1 and A_3 substates do not correspond to "dynamic" and "static" contributions to the spectroscopic line. Rather, the Voigt line shape is a reasonable approximation to the true absorption line shape that is neither Gaussian nor Lorentzian. The 1–2 vibrational bands (*dashed lines*) for each substate are also shown in Fig. 2 b because they contribute to the vibrational echo signal (Merchant et al., 2002). The 1–2 bands were obtained by displacing the 0–1 bands by the measured anharmonicity of 25.4 cm^{-1} (Rector et al., 1997a). Recent measurements using 2D vibrational echo spectroscopy show that the line widths of the A_1 0–1 and
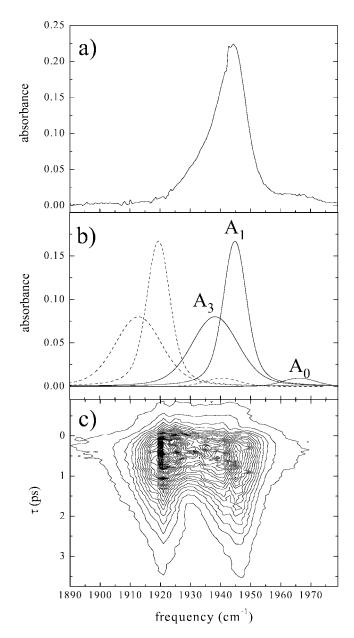

FIGURE 2 Two-dimensional vibrational echo decay at 298 K. (*a*) The background-subtracted linear infrared absorption spectrum of the CO stretch of MbCO. (*b*) Three bands used to fit the absorption spectrum corresponding to the A_0, A_1, and A_3 substates (*solid lines*). The excited state absorption for each band is also shown as a peak shifted to lower energy from the fundamental transition frequency by the anharmonicity of the CO stretch (*dotted lines*). (*c*) A contour plot of the 2D vibrational echo spectrum of MbCO. The vibrational echo decay rate is frequency dependent, reflecting different decay rates for the A_1 and A_3 substates. At 1946 cm^{-1}, the decay is predominantly A_1. At 1931 cm^{-1} the decay is predominantly A_3. The 0–1 and 1–2 dephasing rates for each substate are the same within experimental error.

1–2 bands are the same within experimental error (D. E. Thompson, K. A. Merchant, Q.-H. Xu, and M. D. Fayer, in preparation). It is assumed that, for the A_0 and A_3 transitions, the 0–1 and 1–2 line widths are also the same.

The full 2D time-frequency vibrational echo spectrum was recorded at 298 K and is shown in Fig. 2 *c* as a contour plot. It is clear that different spectral components of the MbCO absorption line have different decay rates. The six bands in Fig. 2 *b* each represent individual contributions to the 1D vibrational echo decay. At this pH, the A_0 band is minimally populated, and it is not discernible in the data presented in Fig. 2 *c*. The 0–1 and 1–2 transitions of the A_1 substate appear at $\sim$1944 cm^{-1} and $\sim$1920 cm^{-1}, respectively. The two transitions have the same decay rate within experimental error. The decay curve is nonexponential, and has a decay constant (1/*e* value) of $\sim$2 ps. The lifetime of the A_1 state was measured with spectrally resolved pump-probe spectroscopy at 298 K and found to be 16.5 ps. Based on the difference between the echo decay rate and lifetime, pure dephasing processes dominate the vibrational echo decay. Because the CO vibrational transition in MbCO is not highly anharmonic, it is not surprising that the 1–2 level has a similar dephasing rate as the 0–1 level. The 0–1 and 1–2 vibrational echo decays of the A_3 substates are also equal to each other within experimental error. The vibrational lifetime of the A_3 substate at 298 K (14.8 ps) makes a negligible contribution to the overall dephasing rate. The A_3 substate vibrational echo signal (contours around 1932 cm^{-1}) decays more rapidly than the A_1 substate (contours around 1946 cm^{-1}).

Figure 3 displays decays that are predominantly the A_1 0–1 decay and the A_3 0–1 decay. The A_1 decay (Fig. 3 *a*) was obtained by taking a slice through the data at 1946 cm^{-1}. At 1946 cm^{-1}, the 0–1 and 1–2 A_0 transitions make a negligible contribution to the vibrational echo signal (see Fig 2 *b*). However, the 0–1 A_3 transition makes a nonnegligible contribution to the signal. The curve in Fig. 3 *a* was obtained by subtracting the contribution of the A_3 line at the polarization level. At the polarization level (square-root of the vibrational echo decays), the signal is linear in the absorption spectrum's amplitude given that the CO transition dipoles for the substates are the same. Based on the relative amplitudes in the linear absorption spectrum of the A_1 and A_3 lines (Fig. 2 *b*), the contribution of the A_3 vibrational echo signal to the decay observed at 1946 cm^{-1} was subtracted out. The intensity level signal of the A_1 substate is obtained by squaring the subtracted polarization level A_1 signal. The details of this procedure are described in Appendix B. The resulting A_1 vibrational echo decay curve (Fig. 3 *a*) is estimated to be >95% pure A_1 decay, based on uncertainty in the line shape fits shown in Fig. 2 *b*. The inset shows the A_1 decay on a semilog plot. The vibrational echo decay of the A_1 substate is nonexponential.

An analogous procedure can be performed for the A_3 decay to remove unwanted contributions from the A_1 line. The primary spectral contaminants to the A_3 decay at this detection wavelength are 0–1 and 1–2 contributions from the A_1 decay. The A_3 decay shown in Fig. 3 *b* was obtained by subtracting off the unwanted contributions, as discussed
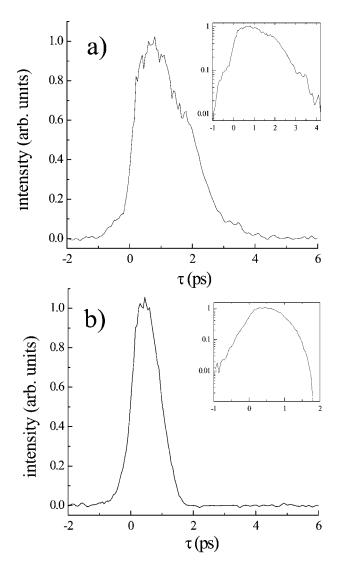

FIGURE 3 Vibrational echo decays of the (*a*) A_1 and (*b*) A_3 substates of MbCO at 298 K. Contributions from overlapping lines have been removed by subtracting off interfering signal contributions at the polarization level. The resulting decays have over 95% of their signal contributions from the A_1 substate (*a*) and the A_3 substate (*b*). The vibrational echo signal from the A_3 substate decays much more rapidly than the echo signal from the A_1 substate. The functional form of the echo decay appears to be different for the two substates. The inset shows each decay on a semilog plot. Both echo decay curves are nonexponential.

in detail in Appendix B. This curve is approximately 95% pure A_3 decay. The vibrational echo decay curve of the A_3 substate is highly nonexponential (see semilog inset). Although these decays may still have some very small residual vibrational echo contributions from different substates, they are overwhelmingly dominated by the decay of the particular line. The ability to accurately subtract off spectral contamination from other lines is dependent on the quality of the fits used to decompose the linear spectrum into the individual substates in Fig. 2 *b*. The sensitivity of the "pure" decay line shapes to errors in subtraction was tested by

varying the amplitude of the subtracted component by 50%. This resulted in only minor changes to the overall shape of the A_1 and A_3 decays, and changed the value of the apparent decay rate by approximately 10%. This is a substantial overestimate of the potential error in the linear spectrum fits. There are two main reasons for the lack of sensitivity to changes in the spectral amplitude of the minor component in the subtraction. First, the unwanted spectral component already has a relatively low amplitude compared to the dominant spectral component at the wavelengths chosen. Second, because the echo signal is proportional to the square of a species' concentration, the dominant spectral contaminant term in the echo decay is typically the cross term between the main spectral component and the interfering spectral component, which is intermediate in character between the two components. Thus, 2D vibrational echo spectroscopy makes it possible to obtain the dephasing dynamics of the individual substates with little interference from the decays of other transitions even when there is some spectral overlap. It is clear from comparisons of Fig. 3, *a* and *b*, that the dephasing dynamics of the A_1 and A_3 substates are very different.

The vibrational echo decays at the two wavelengths used for Fig. 3 were measured at 279 and 320 K in addition to the room-temperature measurements shown in Fig. 3. The signal contributions from the individual substates were isolated at the two detection wavelengths with the same procedure performed on the data in Fig. 3. The results are shown in Fig. 4. The A_1 line (Fig. 4 *a*) shows an appreciable increase in the dephasing rate as the temperature is increased. However, the A_3 (Fig. 4 *b*) shows a much weaker dependence of the dephasing rate on the temperature of the sample over the same temperature range. The freezing point of the aqueous solvent and the denaturation temperature of the protein limit the experimentally accessible temperature range. As can be seen in Figs. 3 and 4, the shapes of the vibrational echo decays for the two substates are quite different.

DISCUSSION

A comparison of the 1D vibrational echo data and 2D vibrational echo data at 298 K clearly shows that the multidimensional vibrational echo technique provides dynamical information that is not obtainable from 1D vibrational echo measurements. In fact, the 1D decays measured with broad bandwidth pulses can be misleading, because, in general, they are a composite of many different decays that can have distinct functional forms and temperature dependences. It is interesting and important to note that the interpretation of the vibrational echo data changes dramatically from the 1D to the 2D scans. The apparent exponential decay of the 1D data implies an extremely rapid decay of the FFCF and motional narrowing of the MbCO dynamic spectral line by the protein's dynamics. However, the 1D echo data is deceptive because the nonexponential form of
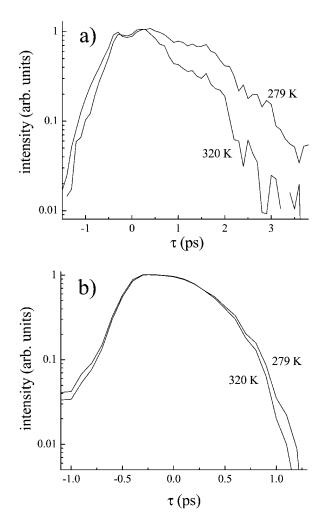

FIGURE 4 Temperature-dependent vibrational echo decays of the A_1 and A_3 substates. (*a*) The A_1 substate echo decay rates at 279 and 320 K increase as the temperature is raised. The vibrational echo decays are not exponential. (*b*) The A_3 substate echo decays at 279 and 320 K [note the different time scales for (*a*) and (*b*)]. The A_3 decays are faster than the A_1 decays at all temperatures. The A_3 decay rate is much less sensitive to temperature than the A_1 decay rate.

the 2D data indicates that a different type of FFCF offers a more reasonable description of the vibrational echo data (Berg et al., 2000). The fact that the different conformational substates of MbCO have different nonexponential dephasing rates was hidden in the 1D experiment. Rector et al. (2001) have shown that a distribution of nonexponential vibrational echo decay rates can lead to the appearance of an overall exponential decay in a 1D vibrational echo scan. Frequency resolving the vibrational echo signal allows the dynamics of the individual substates to be examined separately and permits a closer examination of the dephasing processes that occur in MbCO.

The data in Figs. 3 and 4 demonstrate clearly that the A_1 and A_3 substates have different dephasing rates at room temperature and have dephasing rates with distinct temperature dependences. Despite numerous spectroscopic and
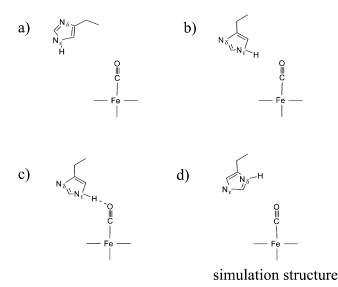
simulation structure

FIGURE 5 Several structures showing possible differences in conformation of the residue His-64 (Phillips et al. 1999). (*a*) The imidazole ring of the His-64 swung out of the pocket away from the CO ligand. (*b*) The N_ε protonated, with a relatively large N_ε–ligand distance. (*c*) The N_ε protonated, with the N_ε–ligand distance closer than in (*b*) with a H-bond between N_ε–H and the ligand. (*d*) Structure with protonated N_δ used in the simulation of the FFCF (Williams et al. 2001).

computational studies (Caughey et al., 1981; Hong et al., 1990; Oldfield et al., 1991; Müller et al., 1999; Phillips et al., 1999; Schulze and Evanseck, 1999; Vojtechovsky et al., 1999; Rovira et al., 2001), the structural origins of the A substates in MbCO remain controversial. In particular, the protonation state of the distal histidine His-64, the proximity and orientation of this residue to the CO ligand, and the absence or presence of a hydrogen bond between the ligand and this residue have all been proposed by various studies to give rise to the different substates. Some of the structures that have been proposed to give rise to the A substates are shown in Fig. 5. In Fig. 5, *a–c*, the N_ε of His-64 is protonated, and in Fig. 5 *d*, the proton is bonded to N_δ. A recent high-resolution crystal structure of MbCO (Vojtechovsky et al., 1999) and several recent computational studies (Phillips et al., 1999; Rovira et al., 2001) have suggested that N_ε is protonated, in contrast to the conclusions of previous x-ray (Kuriyan et al., 1986) and neutron scattering (Cheng and Schoenborn, 1991) data. Recent simulations of MbCO (Schulze and Evanseck, 1999) have also used the tautomer with protonated N_δ. The A_0 substate is generally thought to correspond to the imidazole ring of His-64 being rotated away from the heme pocket as in Fig. 5 *a*, although the protonation state at neutral or high pH is unclear. The origins of the A_1 and A_3 substates are subject to a greater degree of speculation. Phillips et al. (1999) have suggested that the A_1 substate corresponds to a structure with a relatively weak interaction between the imidazole of His-64 and the ligand, as in Fig. 5 *b*, whereas the A_3 substate corre-

sponds to a structure with a smaller residue–ligand distance, possibly with a hydrogen bond, as in Fig. 5 *c*. It has also been suggested that the structural differences between A_1 and A_3 involve other residues in addition to His-64 (Schulze and Evanseck 1999).

The different dephasing dynamics of the A_1 and A_3 substates determined by 2D vibrational echo measurements must reflect the structural differences between these states. Although these data do not by themselves permit an unambiguous structural assignment of the substates, the more rapid dephasing of A_3 relative to A_1 is qualitatively consistent with the assignment of these substates to the structures in Fig. 5, *b* and *c*, respectively.

In principle, calculation of the vibrational echo observable for a model of MbCO with an atomic level of detail requires performing quantum dynamics for thousands of anharmonic degrees of freedom. In practice, classical or semiclassical approximations must be applied. For an anharmonic oscillator interacting with a classical solvent obeying Gaussian statistics, the vibrational echo may be calculated within the fluctuating frequency approximation (Williams and Loring, 2000b; Akiyama and Loring, 2002) from the autocorrelation function of the time-dependent fluctuations in the oscillator frequency FFCF induced by the force on the oscillator coordinate by its surroundings. Williams, et al. (2001) have recently computed the FFCF for sperm whale MbCO in water at 298 K. The frequency fluctuations are assumed to arise from a dynamic Stark effect in which the instantaneous electric field at the ligand from its surroundings induces a transient shift in the vibrational frequency of CO. The electrostatic interaction between the ligand and its surroundings is represented by the coupling of the electric dipole of CO to $\vec{E}(t)$, the total electric field from protein and solvent at the midpoint of the CO bond. The vibrational frequency fluctuation of CO, $\delta\omega(t)$, takes the form (Williams et al. 2001)

$$\delta\omega(t) = (\Delta\mu/\hbar)\,[\vec{E}(t)\times\vec{\mu}(t)-\langle\vec{E}(t)\times\vec{\mu}(t)\rangle], \quad (1)$$

with $\vec{\mu}(t)$ a unit vector along the CO dipole, and $\Delta\mu$ the magnitude of the difference in electric dipole moment between the ground and first excited vibrational states of CO. The angular brackets denote a thermal average. Although $\Delta\mu$ is a quantum mechanical quantity, the ratio $\Delta\mu/h$ has a well-defined classical mechanical limit, which may be related to molecular constants (Williams et al. 2001). The dipole moment difference, $\Delta\mu$, may be measured directly, to within a local field correction (Park et al. 1999), by Stark effect spectroscopy. Park et al. (1999) have determined $\Delta\mu \approx 0.14$ D for CO in a variety of Mb mutants and other heme containing compounds. Williams et al. (2001) have used this value of $\Delta\mu$ together with molecular dynamics simulations of the fluctuating electric field at the ligand in MbCO to compute the FFCF. One molecule of sperm whale MbCO in a solvent of discrete, rigid water molecules was

simulated using the program MOIL (Meller and Elber, 1998). His-64 was assumed to exist in the tautomer with N_δ protonated, and the imidazole ring took on the orientation shown in Fig. 5 *d*.

The simulations produced two spectroscopically distinct species of MbCO: one with a single water molecule in the heme pocket and one without any waters in the pocket. Although these two species had different FFCFs, the echo signals from the two species are very similar, so only the structure without a heme pocket water is considered here. In agreement with previous simulations of heme pocket dynamics in MbCO (Schulze and Evanseck, 1999), the imidazole of His-64 assumed configurations with a relatively large distance from the ligand, which were assumed to correspond to substate A_0, and configurations similar to that in Fig. 5 *d*, which were assumed to correspond to A_1/A_3. Also, in common with previous simulations (Rovira et al., 2001), no separate identification of A_1 and A_3 substates was possible. The decay of the FFCF for A_1/A_3 was dominated at short times (<400 fs) by dynamics of His-64, which were uncorrelated from dynamics of the rest of the protein and the water solvent. On longer timescales (<30 ps), the FFCF reflected correlated dynamics of the rest of the protein and of the water. The A_1/A_3 FFCF was well fit to the functional form of a biexponential decay plus a constant reflecting dynamics that are essentially static on the simulation time scale,

$$\langle \delta\omega(t)\delta\omega(0)\rangle = \Delta_1^2 \exp{(-t/\tau_1)} + \Delta_2^2 \exp{(-t/\tau_2)} + \Delta_0^2,$$

(2)

with $\Delta_1 = 2.07$ ps^{-1}, $\Delta_2 = 1.14$ ps^{-1}, $\Delta_0 = 0.67$ ps^{-1}, $\tau_1 = 0.14$ ps, and $\tau_2 = 4.95$ ps.

The functional form for the FFCF given in Eq. 2 was used to calculate the vibrational echo signal, including the effects of laser pulse shapes, using the procedure described in Appendix A. The resulting echo signal is shown by the solid curves in Fig. 6, in which it is compared to the experimental A_1 signal (*dashed curve*) in Fig. 6 *a* and to the experimental A_3 signal (*dashed curve*) in Fig. 6 *b*. The simulated signal decays more rapidly than either measured signal, but it is closer to that of the A_3 vibrational echo decay. The simulation results show qualitative agreement with both A_1 and A_3 signals. Figure 6 represents a rigorous comparison of calculation and experiment, because no adjustable parameters have been used. Four scenarios, separately or in combination, may explain the absence of distinct A_1 and A_3 substates in the simulation data. First, CO dephasing with protonated N_δ on His-64 as in Fig. 5 *d* may be qualitatively different from dephasing with the N_ε protonated as in Fig. 5 *c*. We are currently recalculating the FFCF for a model with protonated N_ε. Second, other aspects of the empirical force field used in the simulation may preclude the identification of separate A_1 and A_3 substates. Third, our model of the coupling of the CO to its environment through a purely electrostatic dipole mechanism may be incomplete. Fourth,
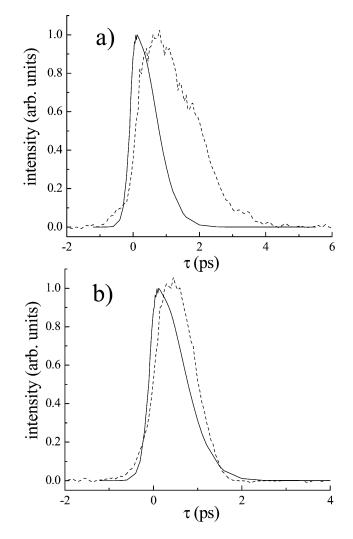

FIGURE 6 Comparison between the calculated vibrational echo decay (*solid lines*) calculated with the FFCF of the A_1/A_3 state of sperm whale MbCO derived from molecular dynamics simulations and the measured A_1 (*dashed line* in *a*) and A_3 (*dashed line* in *b*) vibrational echo decays. The calculation has no adjustable parameters. The calculated vibrational echo decay rate differs by less than a factor of 3 from the A_1 or A_3 decay rates.

our dynamics simulation may not efficiently sample all spectroscopically relevant conformational structures of MbCO on a practical time scale.

The debate in the literature over the structural origins of the A_1 and A_3 conformational substates is over twenty years old. One reason for this is that the only calculation that could be done to test a hypothesis was to compute a vibrational frequency. The 2D vibrational echo provides new information for assessing the accuracy of computational studies of protein dynamics. Proposed structures can be tested not only by whether they produce the correct trends in vibrational frequency but also by whether they give rise to the correct relative dephasing rates and temperature dependences. The added dimension of agreement with dynamical data and structural data can provide additional rigor for computational studies that seek a molecular understanding of proteins.

CONCLUDING REMARKS

The 1D and 2D ultrafast infrared vibrational echo decays of the A_1 and A_3 substates of MbCO were measured at 279, 298, and 320 K. The vibrational echo decay rate for the A_3 state is found to be substantially faster than the A_1 decay rate at each temperature. In addition, the vibrational echo decay rate of the A_1 state is found to increase appreciably as the temperature is raised. The A_3 substate shows a much weaker dependence of the decay rate on temperature. The measured decays are nonexponential, in contrast to 1D vibrational echo measurements made at the same temperatures on the same sample. Multidimensional vibrational echo techniques can reveal a variety of information about vibrational dynamics that is not obtainable from either the absorption spectrum or 1D vibrational echo techniques.

The vibrational echo data at 298K were compared to a calculated vibrational echo decay using a FFCF derived from molecular dynamics simulations. The dephasing mechanism is postulated to be a time-dependent Stark shift in the CO transition frequency caused by a fluctuating electric field at the ligand produced by protein structural fluctuations and solvent dynamics. The semi-quantitative agreement between calculations and data without recourse to adjustable parameters indicates that the molecular dynamics simulations qualitatively reproduce protein structural fluctuations on the experimental time scales. Comparisons between measured vibrational echo observables and molecular dynamics simulations can provide rigorous tests for models of protein dynamics and of protein structure.

APPENDIX A: CALCULATION OF THE ECHO SIGNAL FROM MD SIMULATIONS

For vibrational echo experiments with femtosecond IR pulses, the bandwidth of the femtosecond IR pulse is usually broad enough to cover both 0–1 and 1–2 transitions, and a three-level model is necessary to represent the system (Hamm et al. 1998). Transitions to higher vibrational levels do not contribute to the third-order vibrational echo signal, if only the ground state is significantly thermally populated. The detected signal is proportional to the integrated value of the squared modulus of the nonlinear polarization as a function of the delay time τ and is given by (Mukamel 1995)

$$S(\tau) \propto \int_0^\infty \left| P^{(3)}(\tau, t) \right|^2 \, \mathrm{d}t. \qquad (A1)$$

The nonlinear polarization $P^{(3)}(\tau, t)$ is a result of the convolution of the nonlinear response of the system $\Sigma_i R_i(t_3, t_2, t_1)$ with the applied fields $E_i(t)$,

$$P^{(3)}(\tau, t)$$

$$\propto \int_0^\infty \mathrm{d}t_3 \int_0^\infty \mathrm{d}t_2 \int_0^\infty \mathrm{d}t_1 \left(\sum_i R_i(t_3, t_2, t_1) \right) E_3(t - t_3)$$

$$\times E_2(t - t_3 - t_2) E_1^*(\tau + t - t_3 - t_2 - t_1). \qquad (A2)$$

In these calculations, the applied fields $E_i(t)$ are assumed to be Gaussian in shape with a carrier wave $e^{-i\omega t}$ tuned to the transition, and with a full width at half maximum of 140 fs.
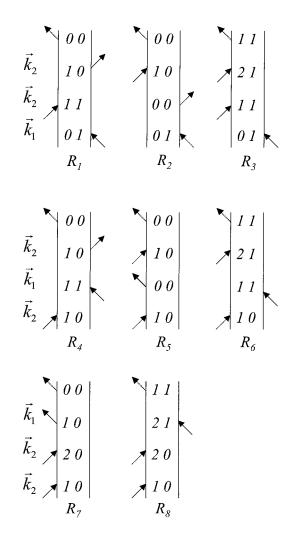

FIGURE A1 Eight Feynman diagrams that contribute to the third-order nonlinear polarization in the $2\vec{k}_2 - \vec{k}_1$ phased matched direction after surviving the rotating wave approximation for an anharmonic vibrational system. The response functions R_1, R_2, R_4, and R_5 involve only the v = 0 and v = 1 vibrational quantum states, whereas the remaining response functions involve the v = 0, v = 1, and v = 2 vibrational quantum states. In the calculation of the spectrally resolved echo signal, only R_1, R_2, R_4, R_5, R_7 are included because only these diagrams lead to emission at the fundamental transition frequency.

For a three-level system, eight response functions contribute to the total signal at third-order in the $2\vec{k}_2 - \vec{k}_1$ phase-matched direction (Mukamel 1995). The corresponding Feynman diagrams (Hamm et al. 1998; Hamm and Hochstrasser 2001) for each response function in Liouville space are shown in Fig. A1. The response functions R_1, R_2, and R_3 are echo pathways that contribute to the signal at positive delay times, response functions R_4, R_5, and R_6 are nonrephasing pathways that contribute only near time $\tau = 0$ when the two pulses overlap, and R_7 and R_8 are nonrephasing pathways that contribute to the signal at negative delay times. The frequency of the signal contribution in diagrams R_1, R_2, R_4, R_5, and R_7 is equal to the fundamental transition frequency, ω_0, whereas R_3, R_6, and R_8 have a signal contribution at the frequency $\omega_0 - \Delta$, where Δ is the anharmonicity of the transition. If Δ is large compared to the amount of inhomogeneous line broadening in the system, then it is possible to separate the signal contributions at the two frequencies ω_0 (R_1, R_2, R_4, R_5, and R_7) and $\omega_0 - \Delta$ (R_3, R_6, and R_8) by spectrally resolving the nonlinear signal. Because the

calculated nonlinear signal is being compared to spectrally resolved vibrational echo data at the fundamental transition frequency, only those response functions that contribute to the signal at frequency ω_0 (R_1, R_2, R_4, R_5, and R_7) were included in the calculation.

The expressions for the relevant response functions used in the calculation are given below (Mukamel 1995; Hamm et al. 1998; Hamm and Hochstrasser 2001):

$$R_1 = R_2 = |\vec{\mu}_{10}|^4 \exp[-i\omega_0(t_3 - t_1)]$$
$$\times \exp\left[-\frac{(t_1 + 2t_2 + t_3)}{2T_1}\right]\exp(-g(t_1) + g(t_2)$$
$$- g(t_3) - g(t_2 + t_1) - g(t_3 + t_2) + g(t_1 + t_2 + t_3)),$$
$$(A3a)$$

$$R_4 = R_5 = |\vec{\mu}_{10}|^4 \exp[-i\omega_0(t_1 + t_3)]$$
$$\times \exp\left[-\frac{(t_1 + 2t_2 + t_3)}{2T_1}\right]\exp(-g(t_1) - g(t_2)$$
$$- g(t_3) + g(t_2 + t_1) + g(t_3 + t_2) - g(t_1 + t_2 + t_3)),$$
$$(A3b)$$

$$R_7 = |\vec{\mu}_{10}|^2|\vec{\mu}_{21}|^2 \exp[-i\omega_0 (t_1 + 2t_2 + t_3)]$$
$$\times \exp(i\Delta t_2)\exp\left[-\frac{(t_1 + 2t_2 + t_2)}{2T_1}\right]\exp(g(t_1)$$
$$- g(t_2) + g(t_3) - g(t_2 + t_1) - g(t_3 + t_2)$$
$$- g(t_1 + t_2 + t_3)). \quad (A3c)$$

The line-broadening function $g(t)$ (Mukamel 1995) in Eqs. (A3) is given by

$$g(t) = \int_0^t d\tau_1 \int_0^{\tau_1} d\tau_2 \langle \delta\omega(\tau_2)\delta\omega(0)\rangle, \quad (A4)$$

where $\langle \delta\omega(\tau_2)\delta\omega(0)\rangle$ denotes the FFCF computed classically from molecular dynamics simulations (Williams et al. 2001). The vibrational lifetime $T_1 = 20$ ps was included in the echo calculation. The relations in Eqs. A3 and A4 are based on the following. First, the quantum mechanical FFCF for fluctuations in the 0–1 vibrational transition frequency, $\langle \delta\omega_{10}(\tau)\delta\omega_{10}(0)\rangle$ is approximated by its classical limit, $\langle \delta\omega(\tau)\delta\omega(0)\rangle$. Second, $g(t)$ is assumed to be real-valued, because the absence of a time-dependent spectral shift in this system and in vibrational spectroscopy generally (Hamm et al. 1998) justifies including only the real part of $g(t)$. Third, diagram R_7 involves correlations among fluctuations in the 0–1 and 0–2 transition frequencies. The expression in Eq. A3c is derived by assuming that the fluctuations in the frequencies of the 0–1 and 1–2 transitions are correlated and of identical magnitude (Fourkas et al. 1995; Hamm and Hochstrasser 2001) so that

$$\langle \delta\omega_{20}(\tau)\delta\omega_{20}(0)\rangle = 2\langle \delta\omega_{20}(\tau)\delta\omega_{10}(0)\rangle$$
$$= 2\langle \delta\omega_{10}(\tau)\delta\omega_{20}(0)\rangle$$
$$= 4\langle \delta\omega_{10}(\tau)\delta\omega_{10}(0)\rangle. \quad (A5)$$

In computing the transition dipole moments for the system, the harmonic approximation was used, namely $\sqrt{2}\vec{\mu}_{10} = \vec{\mu}_{21}$ (Rector et al. 1997a; Hamm

et al. 1998). The vibrational lifetime of the $v = 2$ state is assumed to be half as long as the $v = 1$ state (Fourkas et al. 1995).

APPENDIX B: SEPARATION OF THE A_1 AND A_3 ECHO DECAYS

As discussed in Appendix A, the echo signal intensity is proportional to the absolute value squared of the sum of all polarization components that will give rise to a signal seen by the detector. When calculating the magnitude of the echo signal, in the case of a 1D echo, all response function terms from all frequencies in the linear spectrum must be considered. In a 2D spectrally resolved vibrational echo experiment, only polarization contributions from those response functions that lead to emission at the detected wavelength need be considered. If the sample has polarization contributions from two well-resolved transitions, then spectrally resolved vibrational echoes permit independent measurements of the various contributions. Contributions to the total polarization can be separated based on their frequency. If, however, the sample contains spectroscopic transitions that overlap to some extent, then frequency resolution does not completely separate the various contributions to the polarization. In a linear absorption experiment, overlapping band contributions can be separated by linearly subtracting the unwanted spectral component from the desired one. This is possible because the total absorption depends linearly on the sum of the individual contributions to the absorption, $A_{total}(\omega) = \sum A_i(\omega)$. The nonlinear vibrational echo spectrum depends on the absolute value squared of the sum of the individual contributions, $S(\tau, \omega) \propto |\sum P_i(\tau, \omega)|^2$. Cross-terms between the individual polarization components are produced, which makes a linear subtraction inappropriate. However, in certain situations, it is still possible to separate the total echo signal into its individual components when there is some overlap of spectral lines. Taking the square root of $S(\tau, \omega)$ gives the absolute value of the total polarization. If the amplitude and relative phases of the individual contributions to the total polarization can be determined, then the unwanted polarization components can be subtracted off, and the result can then be squared to give the echo decay for a single spectroscopic transition.

In the case of the overlapping A_1 and A_3 substates of MbCO, such a separation is possible. Based on the spectral decomposition in Fig. 2 b approximately 75% of the linear spectrum at 1946 cm^{-1} is due to the A_1 line, whereas the remaining contribution is almost all A_3. The echo signal at 1946 cm^{-1} at the polarization level takes the form

$$|P_{total}| = |P_{0-1}^{A_1} + P_{0-1}^{A_3}|. \quad (B1)$$

Making the reasonable assumption that the transition dipole moments of the A_1 and A_3 substates are essentially identical, the ratio of the polarizations of the A_1 and A_3 substates is equal to the ratio of their concentrations, which is given by their relative intensities in the linear spectrum. Assuming further that the anharmonicities of the A_1 and A_3 substates are virtually identical, there is no phase difference between the individual polarization components for the A_1 and A_3 substates. Provided that the A_3 decay at the polarization level can be determined, its contribution to the total polarization can be subtracted off, leaving only A_1, which can then be squared to give the "pure" A_1 echo decay.

The procedure used to determine the pure A_3 echo decay function is conceptually the same as the one used to isolate the A_1 decay. From the fits in Fig. 2 b, the spectroscopic line at 1932 cm^{-1} is ≈70% A_3. The remaining contributions to the polarization are split equally between the 0–1 and 1–2 transitions of the A_1 line. At the polarization level, the echo signal takes the form

$$|P_{total}| = |P_{0-1}^{A_3} + P_{0-1}^{A_1} + P_{1-2}^{A_1}|. \quad (B2)$$

The 0–1 polarization contribution from the A_1 line has zero relative phase difference with the A_3 polarization term. However, the relative phase of the 1–2 polarization contribution evolves in time relative to the 0–1 polariza-

tion contributions from the A_1 and A_3 line at a frequency equal to the anharmonicity. Subtracting the 0–1 polarization contribution of the A_1 line from the polarization level signal at 1932 cm^{-1} is exactly analogous to the subtraction performed at 1946 cm^{-1} for the A_1 line. Removing the A_1 1–2 contribution is less straightforward. In principle, the 0–1 and 1–2 A_1 contributions can have different decay line shapes and would need to be considered individually. However, a comparison of the 2D data at ~1944 and ~1920 cm^{-1} shows that the 1–2 decay of the A_1 line is, within experimental error, identical in shape to the A_1 0–1 decay. Therefore, the A_1 0–1 echo decay function can be used as the decay function for the 1–2 A_1 contribution to the A_3 data at 1932 cm^{-1}. The initial relative phase difference and subsequent relative phase evolution between the A_1 1–2 polarization and the A_3 0–1 polarization can be determined by accidental degeneracy beats (Merchant et al. 2002) seen in the spectrally resolved echo data (Fig. 2 c) in the region ~1925 cm^{-1}. The net result is the following expression for the total polarization contributions at 1932 cm^{-1}:

$$|P_{\text{total}}| = |P_{0-1}^{A_3} + P_{0-1}^{A_1} + P_{1-2}^{A_1}|$$

$$= |P_{0-1}^{A_3} + P_{0-1}^{A_1}(1 + \cos(\Delta\tau + \phi))|, \quad \text{(B3)}$$

where Δ is the anharmonicity and ϕ is the initial phase of the beat determined from the data. $P_{1-2}^{A_1}$ has the same amplitude and decay profile as $P_{0-1}^{A_1}$, and therefore it factors with $P_{0-1}^{A_1}$ leaving only its phase evolution relative to the other polarization terms. If $P_{0-1}^{A_1}$ is known, it can be subtracted from the total polarization Eq. B1 and then squared, yielding a pure A_3 echo decay.

The procedure outlined above requires that a pure decay of at least one of the A_1 or A_3 substates is available. In the MbCO data here, there is no pure decay, because there is always some overlap between the A_1 and A_3 substates. This difficulty is overcome by performing the subtractions iteratively. As a first approximation, the echo decay curve at 1946 cm^{-1} is assumed to be pure A_1. This is used to compute an enriched A_3 substate echo decay at 1932 cm^{-1}. Although this enriched A_3 substate still has some residual A_1 contributions that were not subtracted out correctly, it does have a higher A_3/A_1 content relative to the echo decay curve at 1932 cm^{-1}. This A_3 enriched curve is then taken to be a pure A_3 decay, which is used to compute a pure A_1 curve. This new A_1 curve is then used to recompute a pure A_3 decay from the data at 1932 cm^{-1}. Subsequent iterations do not change the results, given the noise in the echo data and uncertainties in the spectral decomposition in Fig. 2 b. For each substate, there are only very minor changes in the decay functional form between iterations. A value of $\Delta = 25.4$ cm^{-1} (Rector et al. 1997a) and $\phi = 1.35\pi$ was used in Eq. B3. The subtracted decay curves show little sensitivity to the value of the initial phase, ϕ, used. This procedure is estimated to give decays that are at least 95% pure echo decays for each substate.

When calculating the square of the polarization $|P|^2 = S$ or the square root of the echo decays $\sqrt{S} = |P|$, it is desirable to preserve the original sign of the data to avoid introducing artificial baseline offsets when the data is fluctuating between positive and negative values about the average value of zero. Therefore, the square of the polarization was computed as $S(\tau) = P(\tau)^3/|P(\tau)|$ and the square root of the echo decay was computed as $|P(\tau)| = |S(\tau)|^{3/2}/S(\tau)$.

References

Abella, I. D., N. A. Kurnit, and S. R. Hartmann. 1966. Photon echoes. *Phys. Rev.* 141:391–406.

Akiyama, R., and R. F. Loring. 2002. Vibrational echoes for classical and quantum solutes. *J. Chem. Phys.* 116:4655–4664.

Berg, M. A., K. D. Rector, and M. D. Fayer. 2000. Two-pulse echo experiments in the spectral diffusion regime. *J. Chem. Phys.* 113:3233–3242.

Bodenhausen, G., R. Freeman, G. A. Morris, and D. L. Turner. 1978. NMR-spectra of some simple spin systems studied by 2-dimensional Fourier transform of spin echoes. *J. Mag. Res.* 31:75–95.

Caughey, W. S., H. Shimada, M. C. Choc, and M. P. Tucker. 1981. Dynamic protein structures: infrared evidence for four discrete rapidly interconverting conformers at the carbon monoxide binding site of bovine heart myoglobin. *Proc. Natl. Acad. Sci. U.S.A.* 78:2903–2907.

Cheng, X., and B. P. Schoenborn. 1991. Neutron diffraction study of carbonmonoxymyoglobin. *J. Mol. Biol.* 220:381–399.

Elber, R., and M. Karplus. 1987. Multiple conformational states of proteins: a molecular dynamics analysis of myoglobin. *Science.* 235:318–321.

Fourkas, J. T., H. Kawashima, and K. A. Nelson. 1995. Theory of nonlinear optical experiments with harmonic oscillators. *J. Chem. Phys.* 103:4393–4407.

Golonzka, O., M. Khalil, N. Demirdoven, and A. Tokmakoff. 2001. Coupling and orientation between anharmonic vibrations characterized with two-dimensional infrared vibrational echo spectroscopy. *J. Chem. Phys.* 115:10814–10828.

Hahn, E. L. 1950. Spin echoes. *Phys. Rev.* 80:580–594.

Hamm, P., and R. M. Hochstrasser. 2001. Structure and dynamics of proteins and peptides: femtosecond two-dimensional infrared spectroscopy. *In* Ultrafast Infrared and Raman Spectroscopy. M. D. Fayer, editor. Marcel Dekker, Inc. New York. 273–347.

Hamm, P., M. Lim, and R. M. Hochstrasser. 1998. Non-Markovian dynamics of the vibrations of ions in water from femtosecond infrared three-pulse photon echoes. *Phys. Rev. Lett.* 81:5326–5329.

Hong, M. K., D. Draunstein, B. R. Cowen, H. Frauenfelder, I. E. T. Iben, J. R. Mourant, P. Ormos, R. Scholl, A. Schulte, P. J. Steinbach, A. Xie, and R. D. Young. 1990. Conformational substates and motions in myoglobin. *Biophys. J.* 58:429–436.

Johnson, J. B., D. C. Lamb, H. Frauenfelder, J. D. Müller, B. McMahon, G. U. Nienhaus, and R. D. Young. 1996. Ligand binding to heme proteins. 6. Interconversion of taxonomic substates in carbonmonoxymyoglobin. *Biophys. J.* 71:1563–1573.

Kendrew, J. C. 1948. Preliminary x-ray data from horse and whale myoglobin. *Acta Cryst.* 1:336.

Kubo, R. 1961. A stochastic theory of line-shape and relaxation. *In* Fluctuation, Relaxation and Resonance in Magnetic Systems. D. Ter Haar, editor. Oliver and Boyd, London. 23–68.

Kuriyan, J. W., M. Karplus, and G. A. Petsko. 1986. X-ray structure and refinement of carbon-monoxy (Fe II)-myoglobin at 1.5 Å resolution. *J. Mol. Biol.* 192:133–154.

Lukin, J. A., V. Simplaceanu, M. Zou, N. T. Ho, and C. Ho. 2000. NMR reveals hydrogen bonds between oxygen and distal histidines in oxyhemoglobin. *Proc. Natl. Acad. Sci. U.S.A.* 97:10354–10358.

Meller, J., and R. Elber. 1998. Computer simulations of carbon monoxide photodissociation in myoglobin: structural interpretation of the B states. *Biophys. J.* 74:789–802.

Merchant, K. A., D. E. Thompson, and M. D. Fayer. 2001. Two-dimensional time-frequency ultrafast infrared vibrational echo spectroscopy. *Phys. Rev. Lett.* 86:3899–3902.

Merchant, K. A., D. E. Thompson, and M. D. Fayer. 2002. Accidental degeneracy beats: a new beat phenomenon in non-linear optical spectroscopy. *Phys. Rev. A.* 65:023817(16).

Miller, L. M., M. Patel, and M. R. Chance. 1996. Identification of conformational substates in oxymyoglobin through the pH-dependence of the low-temperature photoproduct yield. *J. Am. Chem. Soc.* 118:4511–4517.

Mukamel, S. 1995. Principles of Nonlinear Optical Spectroscopy. Oxford University Press, New York.

Müller, J. D., B. H. McMahon, E. Y. T. Chen, S. G. Sligar, and G. U. Nienhaus. 1999. Connection between the taxonomic substates of protonation of histidines 64 and 97 in carbonmonoxy myoglobin. *Biophys. J.* 77:1036–1051.

Oldfield, E., K. Guo, J. D. Augspurger, and C. E. Dykstra. 1991. A molecular model for conformational substates in heme proteins. *J. Am. Chem. Soc.* 113:7537–7541.

Park, E., S. Andrews, and S. G. Boxer. 1999. Vibrational stark spectroscopy in proteins: a probe and calibration for electrostatic fields. *J. Phys. Chem.* 103:9813–9817.

Phillips, G. N., Jr., M. L. Teodoro, T. Li, B. Smith, and J. S. Olson. 1999. Bound CO is a molecular probe of electrostatic potential in the distal pocket of myoglobin. *J. Phys. Chem. B* 103:8817–8829.

Rector, K. D., and M. D. Fayer. 1998. Vibrational dephasing mechanisms in liquids and glasses: vibrational echo experiments. *J. Chem. Phys.* 108:1794–1803.

Rector, K. D., and M. D. Fayer. 1999. Myoglobin dynamics measured with vibrational echo experiments. *Laser Chem.* 19:19–34.

Rector, K. D., J. R. Engholm, J. R. Hill, D. J. Myers, R. Hu, S. G. Boxer, D. D. Dlott, and M. D. Fayer. 1998. Dynamics of myoglobin-CO with the proximal histidine removed: vibrational echo experiments. *J. Phys. Chem. B.* 102:331–333.

Rector, K. D., J. R. Engholm, C. W. Rella, J. R. Hill, D. D. Dlott, and M. D. Fayer. 1999. A dynamical transition in the protein myoglobin observed by infrared vibrational echo experiments. *J. Phys. Chem. A.* 103:2381–2387.

Rector, K. D., J. Jiang, M. Berg, and M. D. Fayer. 2001. Effects of solvent viscosity on protein dynamics: infrared vibrational echo experiments and theory. *J. Phys. Chem. B.* 105:1081–1092.

Rector, K. D., A. S. Kwok, C. Ferrante, A. Tokmakoff, C. W. Rella, and M. D. Fayer. 1997a. Vibrational anharmonicity and multilevel vibrational dephasing from vibrational echo beats. *J. Chem. Phys.* 106:10027–10036.

Rector, K. D., C. W. Rella, A. S. Kwok, J. R. Hill, S. G. Sligar, E. Y. P. Chien, D. D. Dlott, and M. D. Fayer. 1997b. Mutant and wild type myoglobin-CO protein dynamics: vibrational echo experiments. *J. Phys. Chem. B.* 101:1468–1475.

Rovira, C., B. Schulze, M. Eichinger, J. D. Evanseck, and M. Parrinello. 2001. Influence of the heme pocket conformation on the structure and vibrations of the Fe–CO bond in myoglobin: a QM/MM density functional study. *Biophys. J.* 81:435–445.

Sagnella, D. E., J. E. Straub, D. Thirumalai, T. A. Jackson, and P. A. Anfinrud. 1999. Vibrational population relaxation of carbon monoxide in the heme pocket of carbonmonoxy myoglobin: comparison of time-resolved mid-IR absorption experiments and molecular dynamics simulations. *Proc. Natl. Acad. Sci. U.S.A.* 96:14324–14329.

Schmidt-Rohr, K., and H. W. Spiess. 1994. Multidimensional Solid-State NMR. Academic Press, London.

Schulze, B. G., and J. D. Evanseck. 1999. The structural, dynamic, and electronic roles of His64 and Arg45 in the spectroscopic A-states of carbonmonoxy myoglobin: multiple molecular dynamics simulations, multivariate analysis and quantum mechanical computations. *J. Am. Chem. Soc.* 121:6444–6454.

Shimada, H., and W. S. Caughey. 1982. Dynamic protein structures. *J. Biol. Chem.* 257:1893–1900.

Thompson, D. E., K. A. Merchant, and M. D. Fayer. 2001. Two-dimensional ultrafast infrared vibrational echo studies of solute–solvent interactions and dynamics. *J. Chem. Phys.* 115:317–330.

Tokmakoff, A., and M. D. Fayer. 1995. Homogeneous vibrational dynamics and inhomogeneous broadening in glass-forming liquids: infrared photon echo experiments from room temperature to 10 K. *J. Chem. Phys.* 103:2810–2826.

Vojtechovsky, J., K. Chu, J. Berendzen, R. M. Sweet, and I. Schlichting. 1999. Crystal structures of myoglobin–ligand complexes at near atomic resolution. *Biophys. J.* 77:2153–2174.

Williams, R. B., and R. F. Loring. 2000a. Classical mechanical photon echo of a solvated anharmonic vibration. *J. Chem. Phys.* 113:1932–1941.

Williams, R. B., and R. F. Loring. 2000b. Computing the classical mechanical vibrational echo with the fluctuating frequency approximation. *J. Chem. Phys.* 113:10651–10662.

Williams, R. B., R. F. Loring, and M. D. Fayer. 2001. Vibrational dephasing of carbonmonoxy myoglobin. *J. Phys. Chem. B.* 105:4068–4071.

Zanni, M. T., S. Gnanakaran, J. Stenger, and R. M. Hochstrasser. 2001. Heterodyned two-dimensional infrared spectroscopy of solvent-dependent conformations of acetylproline-NH2. *J. Phys. Chem. B.* 105:6520–6535.

Zimdars, D., A. Tokmakoff, S. Chen, S. R. Greenfield, M. D. Fayer, T. I. Smith, and H. A. Schwettman. 1993. Picosecond infrared vibrational echoes in a liquid and glass using a free electron laser. *Phys. Rev. Lett.* 70:2718–2721.